

**SiC-YiG X band quantum sensor for
Sensitive Surface Paramagnetic Resonance
applied to chemistry, biology, physics.**

Jérôme TRIBOLLET

*Institut de Chimie de Strasbourg, Strasbourg University, UMR 7177 (CNRS-UDS),
4 rue Blaise Pascal, CS 90032, F-67081 Strasbourg Cedex, France
E-mail : tribollet@unistra.fr*

ABSTRACT

Here I present the SiC-YiG Quantum Sensor, allowing electron paramagnetic resonance (EPR) studies of monolayer or few nanometers thick chemical, biological or physical samples located on the sensor surface. It contains two parts, a 4H-SiC substrate with many paramagnetic silicon vacancies (V_2) located below its surface, and YIG ferrimagnetic nanostripes. Spins sensing properties are based on optically detected double electron-electron spin resonance under the strong magnetic field gradient of nanostripes. Here I describe fabrication, magnetic, optical and spins sensing properties of this sensor. I show that the target spins sensitivity is at least five orders of magnitude larger than the one of standard X band EPR spectrometer, for which it constitutes, combined with a fiber bundle, a powerful upgrade for sensitive surface EPR. This sensor can determine the target spins planes EPR spectrum, their positions with a nanoscale precision of ± 1 nm, and their 2D concentration down to $1/(20\text{nm})^2$.

SiC-YiG X band quantum sensor. (J. Tribollet - 01/2019)

Electron paramagnetic resonance¹ (EPR) investigation of electron spins localized inside, at surfaces, or at interfaces of ultrathin films is highly relevant. In the fields of photovoltaic² and photochemistry³, EPR is useful to study the spins of photo-created electron-hole pairs, their dissociation, and their eventual transport or chemical reaction occurring at some relevant interface. In opto-electronics with 2D semiconductors⁴, spins of defects limiting device performance can be identified and quantified by EPR. In magnetic data storage science⁵ and in spin-based quantum computing science using molecules⁶ grafted, tethered, encapsulated or physisorbed on a solid substrate, it is relevant to study by EPR the magnetic properties of those molecules, always modified by their interaction with the substrate⁷. In solid supported heterogeneous catalysis, it is relevant to study spins involved in catalytic reactions, using EPR⁸ and eventually spin trapping methods⁹. In structural biology, it is relevant to study by EPR spin labeled proteins^{10,11} introduced in polymer supported or tethered lipid bilayers membranes^{12,13}. In the context of the development of new theranostic agents for nanomedicine, it is relevant to study ligand-protein molecular recognition events occurring on surfaces by EPR, using for example, bifunctional spin labels¹⁴. As various nanotechnologies now allow to produce nanoscale thickness samples, one needs to perform sensitive Surface EPR (S-EPR). However, commercial EPR spectrometers have not enough sensitivity¹⁵ for EPR study of those few monolayers thick ultra-thin films, particularly when target spins are diluted and when samples stacking is not possible.

Home-made EPR experimental setups have been developed recently, in the context of quantum sensors¹⁶⁻²⁰ and quantum computers, reaching single spin sensitivity by optically^{17,18,21}, electrically²² or mechanically²³ detected EPR. Some of them achieved the nanoscale resolution imaging, when combined with magnetic devices moving over surfaces^{24,25}. Other recent advances in the field of inductively detected EPR have also considerably improved sensitivity, but at the price of operating home-made microwave devices at unconventional millikelvin temperatures²⁶. Thus, clearly, there is today a gap between performances of standard X band EPR spectrometers already used worldwide by most of chemists, biologists and physicists, and the ones of the bests unconventional EPR setups found in just few laboratories worldwide.

Here I present the theory of a new Optically Detected Magnetic Resonance (ODMR) based electron spins Quantum Sensor, allowing to study target electron spins of ultrathin paramagnetic samples located on the sensor surface. It has nanoscale resolution in one dimension, a high sensitivity due to spins ensemble ODMR, and importantly, is designed as an upgrade of standard X band pulsed EPR spectrometers. The design of the magnetic properties of the sensor is inspired from the ones of the hybrid paramagnetic-ferromagnetic quantum computer device²⁷ I previously proposed. However, here, it is adapted to constraints of standard X band (10 GHz, 0.35 T, 5 mm sample access) pulsed EPR resonators and spectrometers and thus to fiber bundle based ODMR^{28,29}. The quantum sensor contains two parts. The first is a 4H-SiC semiconductor substrate containing, just below its surface, isolated negatively charged silicon vacancies (V_2) used as quantum coherent ODMR spin probes^{20,21,30,31,45}. The second part is an ensemble of ferrimagnetic YIG (Yttrium Iron Garnet) nanostripes³² having narrow spin wave resonances at X band. A fixed spacer fabricated on edges adjust the relative distance between the two parts. Next, I present the fabrication methodology, magnetic and optical properties, and finally spins sensing properties, based on PELDOR spectroscopy^{1,10,11,18,33}, of this SiC-YiG quantum sensor.

SiC-YiG X band quantum sensor. (J. Tribollet - 01/2019)

The quantum sensor device proposed can be obtained by fabricating its two parts separately and then integrating them (fig.1 a, b). As said in introduction, the first part of the quantum sensor is a 4H-SiC semiconductor sample, in which silicon vacancies spin probes^{20,21,30,31,45} called V_2 are created just below the 4H-SiC surface, and on which the ultra-thin paramagnetic film of interest will have to be deposited, anchored or self assembled (fig.1). This is necessary because the spins sensing principle is related to the many long range dipolar couplings that exist between a given single V_2 spin probe and the many neighbor target spins (fig.1c), those couplings affecting the spin coherence time of V_2 spins probes and being revealed by PELDOR spectroscopy^{1,10,11,18,33}. The 4H-SiC sample can be a 4H-SiC substrate terminated on one side by an isotopically purified 4H-SiC grown layer, having no nuclear spins²¹ and a very low residual n type doping ($< 10^{14} \text{ cm}^{-3}$)²¹. However, a commercially available 4H-SiC substrate with low n doping and a natural low amount of non-zero nuclear spins is also a good starting point.

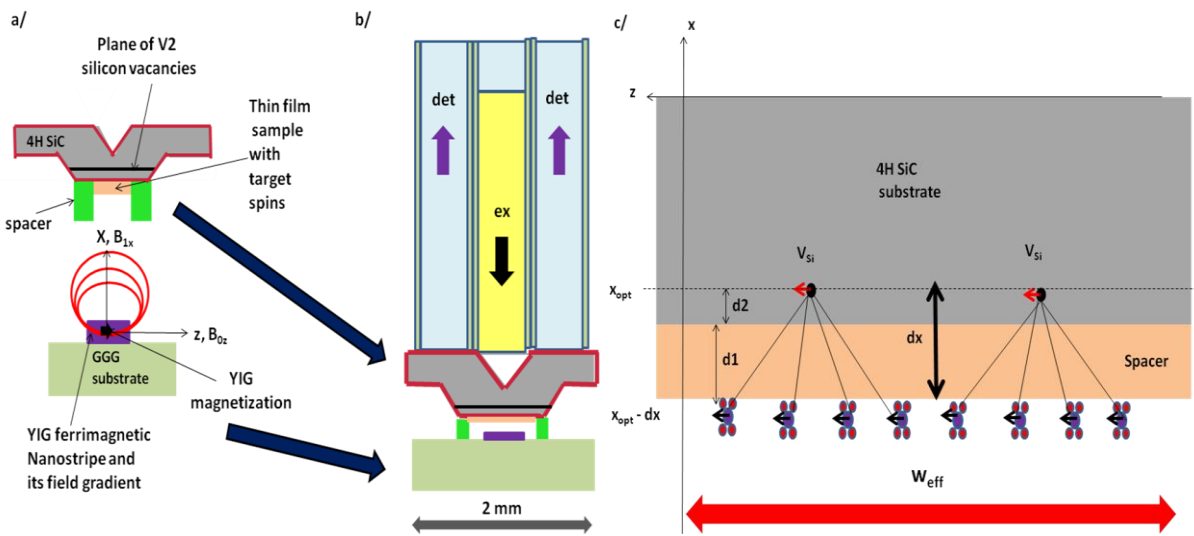


figure 1 : a/ two parts of the Quantum Sensor: the paramagnetic 4HSiC one, with V_2 spins on front side of the truncated cone shape island (45°), and a cone shaped dip (45°) on back side; and the ferrimagnetic one, with many identical YIG nanostructures on GGG substrate (only one stripe shown here for clarity, thus not at scale). Also shown on b/, their integration by a spacer (not at scale) and introduction in a standard pulsed EPR spectrometer microwave cavity, as well as the fiber bundle and the GRIN microlens (yellow) used for fiber bundle based ODMR. b/: Zoom showing the many dipolar couplings (dark lines) existing between V_2 spins probes in 4H-SiC and target spins in the sample, used for quantum sensing by OD PELDOR spectroscopy. Molecular target spins and V_2 probe spins are here separated by a capping layer of few nanometers. w_{eff} indicate the width along z direction over which the dipolar magnetic field produced by a nearby YIG nanostructure can be considered as homogeneous. dx is the distance between the plane of V_2 spins and the plane of target molecular spins considered here. $d_1+d_2=dx$. Orders of magnitude: $C_{2D,V_2}= 1/(30\text{nm})^2$ et $C_{2D,Target}= 1/(5\text{nm})^2$, $dx=10\text{nm}$, et $d_2=2\text{nm}$, $d_1=8\text{nm}$, $w_{eff}=60\text{nm}$ for a nearby YIG nanostructure ($T=100\text{nm}/W=500\text{nm}$), whose center is located at a distance $x_{opt}=150\text{nm}$ here from the V_2 spins plane.

The fabrication process of silicon vacancies V_2 spins probes in 4H-SiC that I propose here is described on top of fig.2. It is based on an implantation-etching approach, combined with SiC sculpting, in order to define the appropriate photonic structure for the optical excitation and detection of V_2 spins probes. After cleaning of the 4H-SiC surface, 5 nm of sacrificial SiO_2 are fabricated on the surface of the 4H-SiC substrate (thickness of $400 \mu\text{m}$). Those 5 nm of SiO_2 can be obtained, either by slow oxidation of the 4H-SiC surface³⁴ into SiO_2 at around 1150°C , or by a lower temperature thin film deposition method like by PECVD³⁵ or atomic layer deposition (ALD)³⁶ at 150°C . High temperature oxidation should

SiC-YiG X band quantum sensor. (J. Tribollet - 01/2019)

advantageously remove residual V_2 silicon vacancies initially present in the 3D bulk of the 4H-SiC sample, as V_2 vacancies are annealed out³¹ at around 700°C. Then, 20 nm of a stopping sacrificial layer of zinc oxide (ZnO) are deposited on top of $\text{SiO}_2/4\text{H-SiC}$, by sputtering or by ALD. Then 22 keV As^+ ions are implanted in this tri-layer sample at a dose comprised between $1.6 \cdot 10^{12} \text{ cm}^{-2}$ and $1.6 \cdot 10^{13} \text{ cm}^{-2}$. The target dose here is around $8.3 \cdot 10^{12} \text{ cm}^{-2}$, which corresponds, according to SRIM simulations (see SI), to a 2D effective concentration of As^+ ions in the first 2 nm of 4H-SiC of $C_{2\text{D}, \text{As}^+} = 1/(32\text{nm})^2$. SRIM simulations also indicate that the concentration of As^+ ions rapidly decay with depth in 4H-SiC and is almost zero after the first 10 nm of 4H-SiC. SRIM simulations also indicate that such implantation of As^+ ions produce 1.3 silicon vacancy per As^+ ion in those first 2 nm of 4H-SiC. One can thus consider that we obtain a 2D effective concentration of silicon vacancies V_2 in the first 2 nm of 4H-SiC of $C_{2\text{D}, \text{eff}, V_2} = 1/(32\text{nm})^2$. This concentration rapidly decays to zero in the next few nanometers in 4H-SiC. Then, 4H-SiC micro-sculpting is performed either by diamond machining^{37,38}, by laser ablation³⁹, by FIB⁴⁰ or by another micromachining method⁴¹. The aim is to produce, on front side, a truncated cone shape island with V_2 spins on top, and on back side, a cone shape dip (cone edge angle of 45° in both cases), both cones sharing the same symmetry axis and having an optical quality surface roughness (fig.2 top). Then, ZnO is etched by HCl, and SiO_2 is etched by HF ⁴². This leads to a sculpted sample with shallow silicon vacancies created mainly 2 nm below the surface of the 4H-SiC truncated cone shape island. A post implantation-sculpting-etching annealing, at a temperature inferior to 600-700°C, can eventually be performed to remove some unwanted created defects. Then, a treatment passivates the truncated cone shape 4H-SiC island surface, like a H+N plasma treatment⁴³ at 400°C, reducing its surface density of state to $6 \cdot 10^{10} \text{ cm}^{-2}$. Then, eventually (not shown on fig.2), a few nm capping layer, easy to functionalize, can be deposited on this passivated 4H-SiC surface, for example using ALD of silicon oxide at low temperature³⁶. Then, a spacer of appropriate thickness, 200 nm here, for example a ring shape spacer made of silicon oxide, is fabricated by standard lithography and deposition, on the edges of the top surface of the 4H-SiC or 4H-SiC/ SiO_2 island, under which the V_2 spins probes were created. The diameter of this top 4H-SiC island surface is around 900 μm . The spacer will allow the integration of the two parts of the quantum sensor device by contacting them (fig.1b). Finally, the few monolayers paramagnetic film of interest can be created on top of the sensor surface. It is either chemically anchored or physically adsorbed on the sensor surface, eventually pre-functionalized. Note also that it is possible to first deposit a nanoscale thickness solid thin film on the sensor surface and then to fabricate a spacer on it, with the appropriate thickness.

The fabrication process of the YIG ferrimagnetic nanostripes array on the GGG (Gadolinium Gallium Garnet) substrate, necessary for the second part of this quantum sensor (fig.2 bottom), follows processes recently published^{32,44}. Those processes were successful in producing YIG nanostructured thin films with narrow spin wave resonances at X band^{32,44}. Shortly, those processes use a reactive magnetron sputtering system operating at room temperature with a YIG target. The deposition has to be done through a mask fabricated on GGG, obtained by electron beam lithography (fig.2 bottom). After the YIG deposition and mask removal, a thermal treatment at around 750-800°C under air flow or oxygen atmosphere, during around 1 or 2 hours, has to be performed^{32,44}.

SiC-YiG X band quantum sensor. (J. Tribollet - 01/2019)

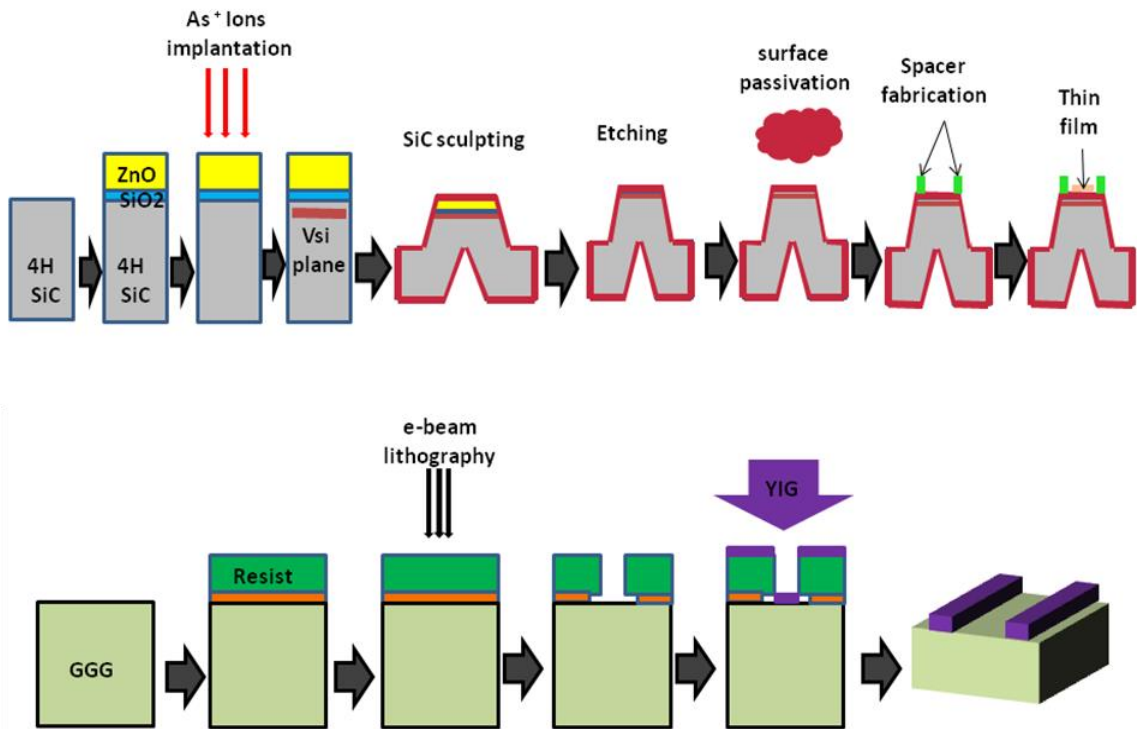


figure 2: Fabrication of the quantum sensor device: 4H-SiC part (top) and YIG/GGG part (bottom); see text for details on the various successive fabrication processes. When possible, and if it is advantageous, the order of some processes can be modified, as long as the key targeted quantum sensor properties are conserved.

Quantum sensing^{16-20,24,25} by optically detected^{17,18,21} PELDOR spectroscopy^{1,10,11,18,33} (fig.5) is only possible if the V_2 spins probes created and coherently manipulated at the microwave probe frequency f_s are sufficiently quantum coherent intrinsically, that is without any nearby target spin bath, in order to be able to feel the added spin decoherence^{1,17,18,24} produced by the spin bath of the sample of study, when it is driven at the microwave pump frequency f_p (fig.5). Let us discuss firstly the electron spin coherence time expected for the spin $S=3/2$ of a 4HSiC silicon vacancy (V_2)^{21,30,31,45} created by this fabrication process few nanometers below the surface. Nuclear spin bath spectral diffusion²¹ is small in 4HSiC which contains very few non-zero nuclear spins, and it can be eliminated by isotopic purification. Bulk electron spin bath spectral diffusion is small in lightly n-doped 4HSiC and can be reduced by chemical purification and doping control²¹. Spin-lattice relaxation should be quite inefficient for V_2 spins probes, in view of the very long spin coherence time of 100 μs observed already at room temperature for bulk V_2 spins probes^{21,30,31}. Spin decoherence induced by the residual paramagnetic states present at the 4H-SiC passivated surface is negligible for most V_2 spin probes, due to the low 2D residual defect concentration after passivation⁴³ ($6.10^{10} \text{ cm}^{-2}$). Thus, the dominant intrinsic decoherence process for V_2 spins probes in this quantum sensor device is expected to be instantaneous diffusion¹ in 2D, occurring among the V_2 spins probes having the same resonant magnetic field, at fixed microwave probe frequency and under the strong dipolar magnetic field gradient produced

SiC-YiG X band quantum sensor. (J. Tribollet - 01/2019)

by the YIG nanostripes. Note that YIG is fully saturated at X band because its saturation field^{32,44} is $B_{sat}=1700$ G and the external B_0 field applied for EPR is around 3500 G.

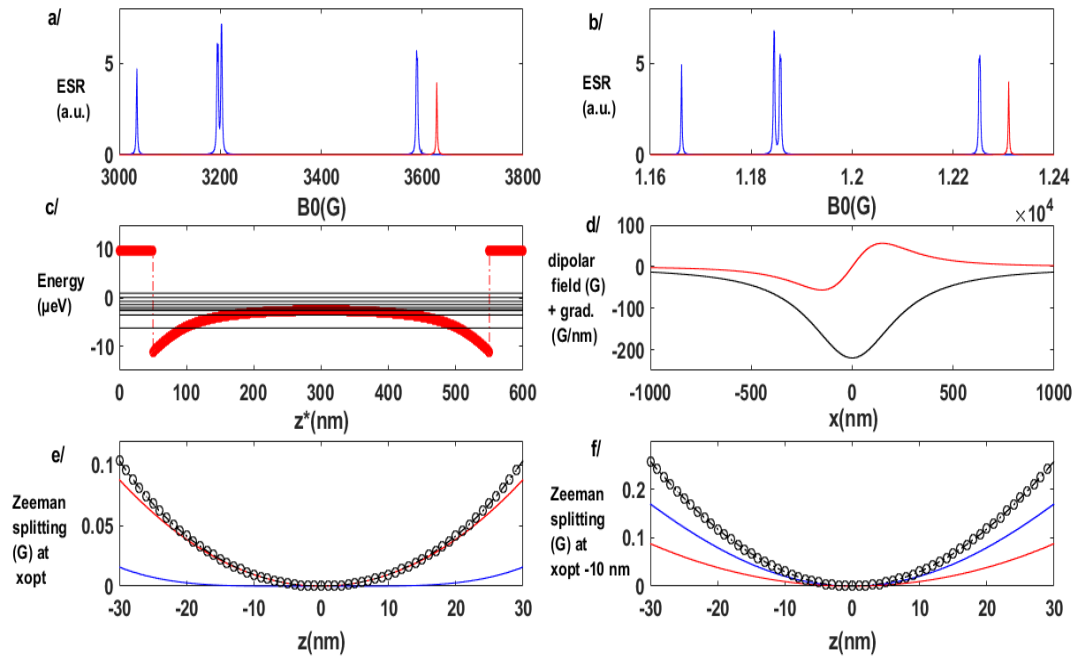


figure 3 : YIG nanostripes magnetic properties assuming the following dimensions, width $W=500$ nm , thickness $T=100$ nm, length $L=100\mu\text{m}$, and $B_{sat}=1700$ G. a/ and b/ Electron spin resonance spectrum at X (9.7 Hz) and Q (34 GHz) band respectively, showing, in blue, the YIG nanostripes spin wave resonances and, in red, the shifted paramagnetic resonance of reference $g=2.00$ electron spins, placed at $x_{opt}=150$ nm above the YIG nanostripe center ($x=0$). Paramagnetic and ferrimagnetic resonances have linewidth of 1 G here. c/ One dimensional eigenenergies of the spin waves along z axis (horizontal lines) represented on top of the inhomogeneous effective confining potential inside a YIG nanostripe saturated along its width (here $z^*=300+z$); $z=0$ corresponds to the center of the stripe . d/ z component of the dipolar magnetic field of the YIG nanostripe as a function of x (black), as well as its gradient along x (red) multiplied here by 100 for clarity. e/ and f/ Total effective Zeeman splitting at X band (dot line), expressed in Gauss (thus divided by $(g \mu_B)$), assuming $g=2.00$), as well as its two contributions: the one of Bdz to first order in blue, and the one of Bdx in red to second order, as produced by the YIG nanostripe, respectively at x_{opt} (e/) and at $x_{opt} - 10$ nm (f/), and both plotted versus z , to show the lateral homogeneity of this effective Zeeman splitting.

The figure 3 summarizes the static and dynamic magnetic properties of the YIG nanostripes. The fig. 3d shows that the maximum magnetic field gradient in the x direction, perpendicular to the GGG and 4HSiC surfaces, is of around 0.5 G/nm and is obtained at a distance $x_{opt}=150$ nm from the center of a given YIG nanostripe. That is why the spacer has to have a thickness of $x_{opt} + T/2 = 200$ nm, such that the V_2 spins probes feel the maximum magnetic field gradient. The magnetic field gradient produced by such a YIG nanostripe is not rigorously one dimensional along x . However, as I previously explained in the context of quantum computing²⁷, locally, around $x_{opt} = 150$ nm here, and laterally at $z=0 \pm 30$ nm along z , detailed calculations clearly show (fig. 3e) that in this portion of plane above each YIG nanostripe, the dipolar magnetic field can be considered as laterally homogeneous with a precision of 0.1 G. Even in the portion of plane located at around $x_{opt} - 10$ nm, and laterally at $z=0 \pm 30$ nm along z , which is a possible position where target spins could be found, the dipolar magnetic field can be considered as laterally homogeneous with a precision of 0.3 G

SiC-YiG X band quantum sensor. (J. Tribollet - 01/2019)

(fig. 3f). As the V_2 spins probes in 4HSiC have a narrow linewidth^{21,30,31,45,46} of less than 1 G, with a gradient here of 0.5 G/nm, one can thus consider that all the V_2 spins probes located between x_{opt} and $x_{opt}-2nm$ (fig 1c), just below the 4HSiC surface, and with $z=0 \pm 30$ nm along z ($w_{eff}=60$ nm), have the same resonant magnetic field with a precision of around 1 G. As their 2D concentration obtained by fabrication is $1/(32nm)^2$, their decoherence time associated to instantaneous diffusion in 2D is numerically calculated to be $T_{ID,2D}= 12.5 \mu s$, and is independent of the temperature. Selective microwave pulses¹ can thus excite this V_2 spins probes plane, without exciting the other more diluted V_2 spins planes located in the next few nanometers of 4HSiC. The V_2 plane - target spins plane distance is thus measured here with a precision of around $\pm 1nm$.

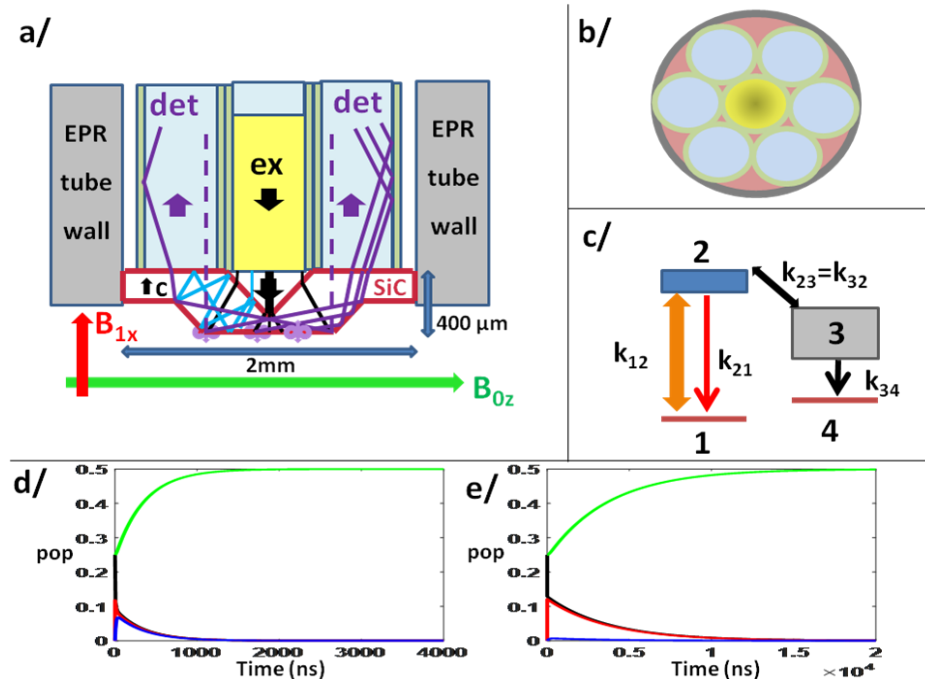


figure 4 : Some optical properties of the quantum sensor described here: a/ ODMR setup: fibers bundle (6+1, in blue), GRIN lens (NA=0.5, 0.25 pitch, diameter: 500 μm , in yellow) for collimation after the central fiber, EPR tube (in gray), and 4H-SiC sculpted sample (edges in red, cone angles are 45°); all are inserted inside a microwave resonator like the MD5 flexline resonator (the YIG part of the sensor, supporting the SiC one, is not shown here for clarity); also shown on a/, static B_{0z} and microwave magnetic field $B_{1x}(t)$, some near surface V_2 electric dipoles aligned along the c axis of 4H-SiC (in violet, maximum emission along the z axis , orthogonal to the c axis), and some relevant optical rays for geometric optics investigation of the excitation and collection efficiencies of this new ODMR based setup for quantum sensing. Blue ray is an optical pumping ray with many TIR on SiC faces. Black rays are also optical pumping rays, but TIR are not shown for clarity. Violet rays are photoluminescence rays emitted at 10° with respect to the horizontal and they are still collected by TIR in lateral fibers (NA=0.44, diameter: 500 μm). See also zoom in SI. b/ section view of the fiber bundle just above the SiC sample. c/Negatively charged silicon vacancy V_2 energy level scheme, explaining the optical readout cycle and the optical pumping cycle. Level names^{31,45,46}: 1: (Ground State, $S=3/2, M_{sz} = -3/2$ (or $+3/2$)), 2: (Excited State) , 3: (Meta-stable excited state) , 4: (Ground State, $S=3/2, M_{sz} = -1/2$ (or $+1/2$)), k_{12} is laser induced optical absorption/emission rate, k_{21} is photoluminescence rate, $k_{23}=k_{32}=k_{ISC}$ is the intersystem crossing rate, k_{34} is a non-radiative relaxation rate. d/ and e/ : Numerical simulations of populations, based on rate equations, showing the optical pumping^{31,45,46} time necessary to saturate the population of V_2 spins in the - 1/2 states (green curve) to its maximum value of 0.5 (Note: one can also show that under such OP, the population of V_2 spins in the + 1/2 state also saturates to 0.5, using a similar energy level scheme and OP/OD cycles). In d/, $k_{23}=k_{32}=1/(17$ ns) at 300K^{31,45,46}, and in e/, $k_{23}=k_{32}=1/(1700$ ns) assumed at 5K, and for both, $k_{21}=1/(6$ ns), $k_{34}=1/(107$ ns), $k_{12sat}=2.6$ ns⁻¹. Populations shown: N_1 in black, N_2 in red, N_3 in blue, N_4 in green. One finds an optical pumping time of around 20 μs at 5K, and 2 μs at 300K, with those parameters.

SiC-YiG X band quantum sensor. (J. Tribollet - 01/2019)

It must be also noted here that microwave driving of any spin wave resonance of the YiG nanostripes of the quantum sensor, during the ODPELDOR sequence used for quantum sensing, would add unwanted decoherence²⁷ to V_2 spins probes. That is why the ferrimagnetic insulating YiG nanostripes were carefully designed here such that there is no spectral overlap between their confined spin wave resonances²⁷ (fig. 3a, b, c), which are narrow in YiG^{32,44}, and the shifted paramagnetic resonances of the V_2 spins probes (fig. 3a, b). Note also that according to my previous theoretical calculation²⁷, thermal fluctuations of YiG do not contribute to decoherence of V_2 spin probes, due to the reduced saturation magnetization of YiG compared to the one of Permalloy previously considered in the context of quantum computing²⁷. Note also that, as instantaneous diffusion is temperature independent and as YiG is still ferrimagnetic at room temperature, this hybrid SiC-YiG quantum sensor can be used in principle between 4K and 300K.

The ODMR at X band of the ensemble of V_2 spins probes used for sensitive quantum sensing, is based on efficient optical pumping^{21,30,31,45,46} (fig. 4 a,c,d,e), as well as on the efficient collection of V_2 spins probes photoluminescence^{21,30,31,45,46} (fig. 4 a,b), by means of a fiber bundle^{28,29}, a small GRIN microlens (fig. 1a,b and fig. 4 a,b), and the many total internal reflexion¹⁹ (TIR) occurring both in the sculpted 4HSiC sample ($n=2.6$) and in the optical fibers (fig 4 a and see also SI). All components of this ODMR setup can be introduced inside standard X band pulsed EPR microwave resonator^{1,29} allowing PELDOR spectroscopy, like the MD5 flexline resonator⁴⁷, which accept EPR tubes with external diameter up to 5 mm.

One can show that the photoluminescence signal S_{pl} , integrated during T by the photodetector, in the ODPELDOR sequence (fig. 5a), is given by (see SI): $S_{pl} = S_0 \cdot (1-f)$, with $S_0 = p_{ex} \cdot p_{coll} \cdot p_{det} \cdot (T/\tau_{V2}) \cdot (N_{V2}/8)$ and f , a function that depends on the parameters: $2 \cdot t_1$, $2 \cdot t_2$, $T_{id,2D}$, td , $C_{2D,T}$, $p_B(f_{pump})$ (see SI for definitions and details). Note that $p_B(f_{pump})$ is equal to 1 when f_{pump} equal the target spins resonant frequency, and 0, when f_{pump} is far off resonance with the target spins resonant frequency. In optimal experimental conditions, the Noise N_{pl} is dominated by optical shot noise, $N_{pl} = (S_{pl}(p_B=0))^{0.5}$. Thus the "net signal" to "noise" ratio R is given by $R = (S_{pl}(p_B=1) - S_{pl}(p_B=0)) / N_{pl}$. The detailed sensitivity analysis of this quantum sensor (see SI) shows, that in optimal experimental conditions, one could obtain the 200 MHz ODPELDOR spectrum shown on fig. 6b (100 points, one point each 2MHz assumed here) in 1.2 s, with a large signal to noise ratio $R=2600$.

The numerically simulated (see SI) spins quantum sensing properties, obtained by ODPELDOR (fig.5a), are shown on fig. 6. The figure 6a presents the shifted field sweep EPR spectrum at 9.7 GHz of V_2 spins probes located at $x_{opt}=150$ nm from YiG nanostripes (in green) and of two kinds of target spins $S=1$ located at $x_{opt}-dx=145$ nm, that is on the sensor surface (in blue and red, see legend for details), as it could be obtained by direct detected EPR, if it would be sensitive enough for Surface Paramagnetic Resonance. The edge spin wave resonance of YiG nanostripes having the highest resonance field at 9.7 GHz has also been added to this spectrum (in pink). The shifted EPR line of V_2 at highest field is chosen here for ODPELDOR, which means that B_{0z} is set to this field resonance value, and f_s is set to 9.7 GHz, while f_{pump} is scanned during ODPELDOR (fig. 5a). The figure 6b shows the resulting expected X band ODPELDOR spectrum versus $f_{pump}-f_s$, scanned over around 200 MHz. The figure 6c indicates how the normalized ODPELDOR net signal to noise ratio (see SI), given by $R/R_{opt} = 1 - V_{Deer}(td, dx, C_{2D,T})$, depends on $1 - V_{Deer}$, V_{Deer} being the DEER¹¹ signal, and thus how it depends on the relative distance dx between spins probes plane and target spins plane, on

SiC-YiG X band quantum sensor. (J. Tribollet - 01/2019)

the target spin plane concentration $C_{2D,T}$, and on time constant t_d . Thus clearly, this SiC-YiG quantum sensor can determine rapidly the target spins plane EPR spectrum and its 2D concentration down to $1/(20\text{nm})^2$, with a sufficiently high net signal to noise ratio, still assuming a V_2 spins probes planar concentration of $1/(32\text{nm})^2$, and an associated instantaneous diffusion decoherence time in 2D of $T_{1D,2D} = 12.5 \mu\text{s}$.

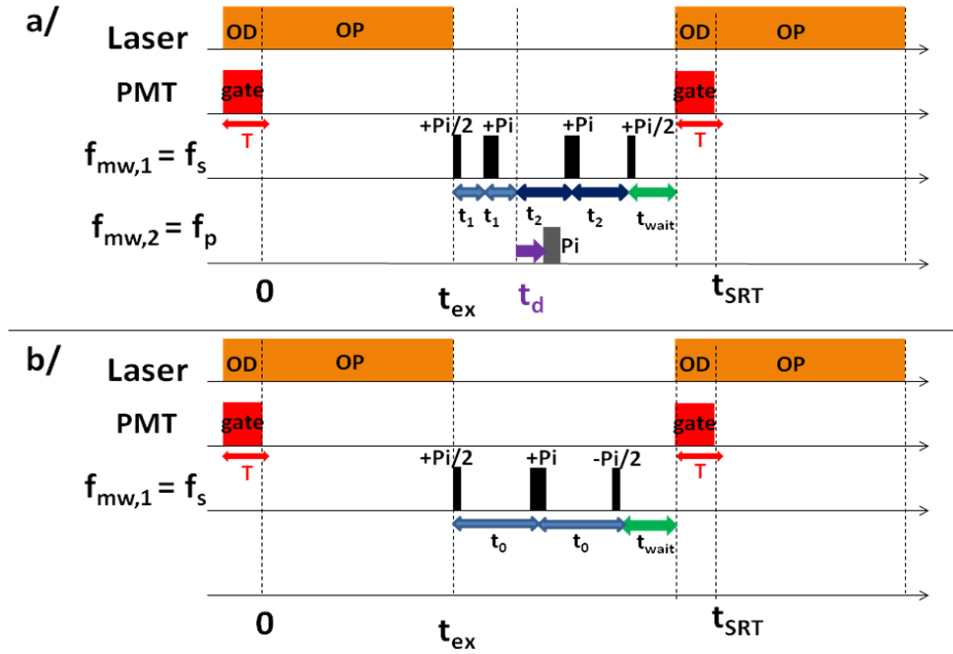


figure 5: a/ X band OD-PELDOR quantum sensing sequence and b/ X band ODMR spin echo decay sequence for characterization of spin coherence time T_2 of V_2 spins probes. The spins states $-1/2$ and $+1/2$ are prepared simultaneously by optical pumping (laser pulse of $100 \mu\text{s}$ assumed here). The microwave probe frequency f_s , and static field B_{0z} , are adjusted to obtain the paramagnetic resonance at this frequency f_s with the chosen optically pumped EPR transition of V_2 probes spins, either $(-3/2 \leftrightarrow -1/2)$, or $(+1/2 \leftrightarrow +3/2)$. Both a/ and b/ time resolved ODMR experiments corresponds nearly to standard PELDOR and Echo Decay experiments¹, but they start after optical pumping and they are complemented by a last $+\pi/2$ pulse in order to transform transverse magnetization M_x ($t_{SRT} - T - t_{wait}$), into populations of V_2 spins, which have different spin dependent photoluminescence and relaxation properties under laser excitation. This allows the final optical detection of EPR, the so-called spins ensemble ODMR, by means for example, of a gated Photomultiplier tube (PMT). As a first approximation here, and to better understand the hybrid optical-microwave pulses sequences, spins states $-1/2$ and $+1/2$ are assumed Dark states, while spins states $-3/2$ and $+3/2$ are assumed Bright photo-luminescent states^{45,46}.

Now I compare the sensitivity of this SiC-YiG fiber bundle based ODMR quantum sensor with other setups. Firstly, it must be noted that the same ODPELDOR spectrum as the one of fig.6b could be obtained also in 1.2 s with a quantum sensor having a single V_2 spin probe, assuming identical experimental parameters, but at the price of a reduced net signal to noise ratio of only $R=2$ (see SI). This new spin ensemble quantum sensor⁴⁸ is thus 1000 times more sensitive than a similar single spin-based quantum sensor. It is thus advantageous in terms of both measurement time and sensitivity. Of course, ensemble measurements imply an additional statistical averaging of target spins plane properties, which is not present in single spin probe measurements, but such statistics is often a relevant information, like in biology^{10,11} and in realistic solid state devices^{5,6}. Also, this spins ensemble quantum sensor has a nanoscale spatial resolution in 1D due to the static gradient

SiC-YiG X band quantum sensor. (J. Tribollet - 01/2019)

used, but no scanning and thus no 3D imaging capabilities, contrary to some scanning single spin sensors. Thus, those two kinds of quantum sensors are quite complementary research

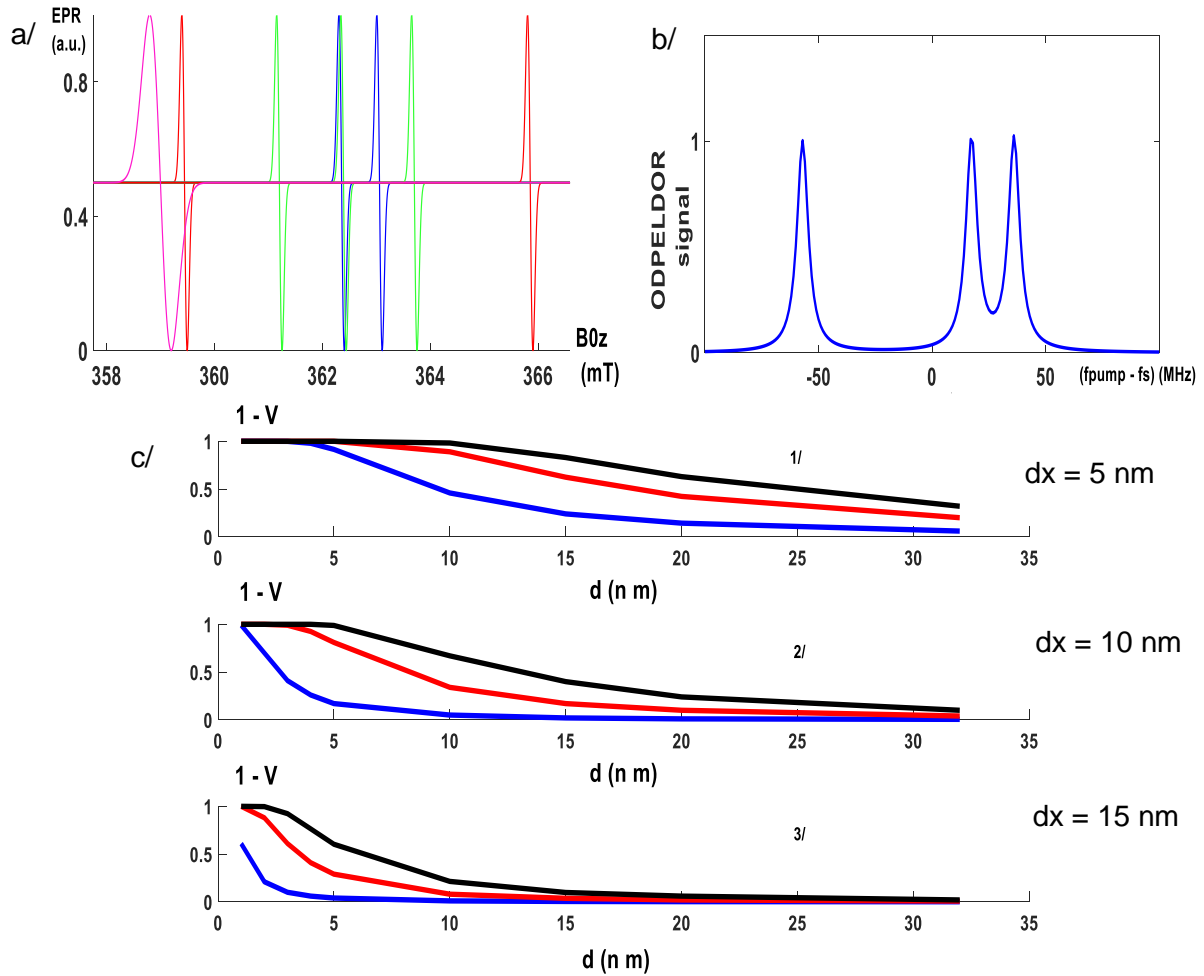


figure 6 : Spins sensing properties of the quantum sensor. a/ The theoretical shifted field sweep EPR spectrum at $f_s = 9.7$ GHz of spins $S=3/2$ of V2 spins probes ($g_{iso}=2.0028$, uniaxial magnetic anisotropy along c axis $D_c = +35$ MHz, C_{3V}) located at $x_{opt}=150$ nm (in green) and of two different ensembles of anisotropic molecular nanomagnets with target spins $S=1$ ($S_1=1$, $g_{iso,1}=2.0028$, $D_{c,1}=20$ MHz, C_{3V} , and $S_2=1$, $g_{iso,2}=2.0028$, $D_{c,2}=180$ MHz, C_{3V}) located at $x_{opt}-dx=145$ nm here, thus on the sensor surface (assuming 3 nm of SiO₂ capping layer). V₂ spins and nanomagnets are assumed here to have their C_{3V} c axis orthogonal to B_{0z}. EPR simulation in a/ performed with Easyspin software. b/ ODPELDOR spectrum versus $f_{pump}-f_s$, associated to spectrum a/, assuming B_{0z} is set equal to the highest EPR resonance of V₂ on a/. c/ Dependence of ODPELDOR normalized net signal to noise ratio (see SI), $R/R_{optimum}=1-V$, on the relative distance dx between spins probes plane and target spins plane ($dx=5$ nm (1/), 10 nm (2/), or 15 nm (3/), from top to bottom), as well as on the target spin plane concentration ($C_{2D,Target}=1/(d^2)$, with d in nm). Dark trace is for $td=5\mu s$, red trace is for $td=3\mu s$, blue trace is for $td=1\mu s$ (see fig.5 for definition of td).

tools. However, this new quantum sensor based on spins probes ensemble, has not only the advantage of being much more sensitive and faster, but also to be compatible with standard X band pulsed EPR spectrometers, such that it should be widely used in a soon future by many researchers, already using standard EPR and who want to improve its performances. The detailed comparison (see SI) of the sensitivity of standard X band direct inductively detected EPR (DD-EPR) with the one of this quantum sensor upgraded EPR (noted here QUSU-EPR), shows that the sensitivity gain on target spins number is at least of five orders of

SiC-YiG X band quantum sensor. (J. Tribollet - 01/2019)

magnitude. It thus clearly allows to perform surface EPR using this quantum sensor combined with a commercial X band pulsed EPR spectrometer and an optical fiber bundle. This quantum sensor upgraded EPR spectroscopy should thus open new research directions, like in the fields of surface chemistry and photovoltaic, in structural biology and nanomedicine, as well as in optoelectronics, spintronics and quantum information processing.

As a last remark, one can note that this theoretical work, as well as the experimental development²⁹ of this hybrid SiC-YiG quantum sensor, can be viewed as intermediate steps towards the future development of an intermediate scale hybrid YiG-SiC spins qubits-based quantum computer, following the guidelines I previously published²⁷. This not scalable quantum computer design could however still be very useful for efficient quantum simulations of new potential molecular drugs⁴⁹. The advantages of this YiG-SiC quantum computer proposal compared to my previous Permalloy-SiC quantum computer proposal are, the narrow spin wave resonances of YiG, the coherent microwave manipulations of SiC spin qubits at the standard X band, optical initialization and optical detection of EPR of spins qubits ensemble, and probably a high operation temperature for SiC spins qubits, some of them remaining quantum coherent over hundred microseconds, even at room temperature^{21,30}.

REFERENCES:

- 1/ **Principles of pulse electron paramagnetic resonance (2001)**. A. Schweiger and G. Jeschke, book from Oxford University Press, Oxford UK; New York (2001).
- 2/ **Time Resolved EPR study of electron-hole dissociations influenced by alkyl side chains at the photovoltaic polyalkylthiophene:PCBM interface**. T. Miura et al., J. Phys. Chem. Lett. (2014), 5, p 30.
- 3/ **EPR investigation of photoinduced radical pair formation and decay to a triplet state in a carotene-porphyrin-fullerene triad**. D. Carbonera et al., J. Am. Chem. Soc. (1998), 120, p 4398.
- 4/ **Paramagnetic intrinsic defects in polycrystalline large-area 2D MoS₂ films grown on SiO₂ by Mo sulfurization**. A. Stesmans et al., Nanoscale Res Lett. (2017), 12, p 283.
- 5/ **Magnetic memory from site isolated Dy (III) on silica materials**. F. Allouche et al., ACS Cent. Sci. (2017), 3, p 244.
- 6/ **A porphyrin spin qubit and its 2D framework nanosheets**. A. Urtizbera et al., Adv. Funct. Mater. (2018), 28, p 1801695.
- 7/ **Probing magnetic excitations and correlations in single and coupled spin systems with scanning tunneling spectroscopy**. M. ternes, Progress in Surface Science (2017), 92, p 83.

SiC-YiG X band quantum sensor. (J. Tribollet - 01/2019)

8/ **EPR characterization and reactivity of surface-localized inorganic radicals and radicals' ions.** M. Chiesa et al., Chem. Rev. (2010), 110, p 1320.

9/ **Electron paramagnetic resonance spectroscopy of catalytic surfaces.** M. Chiesa et al., Chem. Rev. (2010), 110, p 1320.

10/ **Identifying conformational changes with site-directed spin labeling.** W.L. Hubbel et al., Nature Structural Biology (2000), 7, p 735.

11/ **Direct conversion of EPR dipolar time evolution data to distance distributions.** G. Jeschke et al., Journal of Magnetic Resonance (2002), 155, p.72.

12/ **Tethered and polymer supported bilayer lipid membranes: structure and function.** J. Andersson et al., Membranes (2016), 6, 30, p 1-14.

13/ **Polymer supported lipid bilayers.** I. P. McCabe et al., Open Journal of Biophysics (2013), 3, p 59.

14/ **A bifunctional spin label for ligand recognition on surfaces.** M. A. Hollas et al., Angew. Chem. Int. Ed. (2017), 56, p 9449.

15/ **Electron spin resonance probe based on a 100 μm planar microcoil.** G. Boero et al., Review of Scientific Instruments (2003), 74, p 4794.

16/ **Quantum sensing.** C.L. Degen et al., Rev. Mod. Phys. (2017), 89, p 35002.

17/ **Nanoscale sensing using point defects in single crystal diamond: recent progress on nitrogen vacancy center-based sensors.** E. Bernardi et al., Crystals (2017), 7, p 124.

18/ **Sensing external spins with nitrogen-vacancy diamond.** B. Grotz et al., New Journal of Physics (2011), 13, p 55004.

19/ **Broadband magnetometry and temperature sensing with a light-trapping diamond waveguide.** H. Clevenson et al., Nature Physics (2015), 11, p 393.

20/ **Magnetic field and temperature sensing with atomic scale spin defects in silicon carbide.** H. Kraus et al., Scientific Reports (2014), 4, article number: 5303.

21/ **Coherent control of single spins in silicon carbide at room temperature.** M. Widmann et al., Nature Materials (2015), 14, p 164.

22/ **Single shot readout of an electron spin in silicon.** A. Morello et al., Nature (2010), 467, p 687.

23/ **Single spin detection by magnetic resonance force microscopy.** D. Rugar et al., Nature (2004), 430, p 329.

SiC-YiG X band quantum sensor. (J. Tribollet - 01/2019)

24/ **Subnanometer resolution in three-dimensional magnetic resonance imaging of individual dark spins.** M. S. Grinolds et al., Nature Nanotechnology (2014), 9, p 279.

25/ **Nanoscale spin manipulation with pulsed magnetic gradient fields from a hard disc drive writer.** S. Bodenstedt et al., Nano Lett. (2018), 18, p 5389.

26/ **Reaching the quantum limit of sensitivity in electron spin resonance.** A. Bienfait et al., Nature Nanotechnology (2016), 11, p 253.

27/ **Hybrid paramagnetic-ferromagnetic quantum computer design based on electron spin arrays and a ferromagnetic nanostripe.** J. Tribollet, Eur. Phys. J. B. (2014), 87: 183.

28/ **Implementation of optically detected magnetic resonance spectroscopy in a commercial W-band cylindrical cavity.** G. Janssen et al., Rev. Sci. Instrum. (2001), 72, p 4295.

29/ **First experimental developments towards quantum sensing with a standard X band EPR spectrometer and a hybrid paramagnetic-ferrimagnetic quantum sensor device.** J. Tribollet, to appear in 2019.

30/ **Point defects in SiC as a promising basis for single-defect, single-photon spectroscopy with room temperature controllable quantum states.** P.G. Baranov et al., Materials Science Forum (2013), 740-742, p 425.

31/ **Optical spectroscopy on silicon vacancy defects in silicon carbide.** Franziska Fuchs, PhD thesis (2017), Wurzburg University.

32/ **Epitaxial patterning of nanometer-thick $Y_3Fe_5O_{12}$ films with low magnetic damping.** S. Li et al., Nanoscale (2016), 8 (issue 1), p 388.

33/ **Three pulse ELDOR theory revisited.** K.M. Salikhov et al., Appl. Magn. Reson. (2014), 45, p 573.

34/ **Growth rates of dry thermal oxidation of 4H-silicon carbide.** V. Simonka et al., Journal of Applied Physics (2016), 120, p 135705.

35/ **Influence of PECVD of SiO₂ passivation layers on 4H-SiC Schottky rectifiers.** S. Nigam et al., Electrochem. Solid state Lett. (2003), 6, G4-G6.

36/ **Low temperature silicon dioxide by thermal atomic layer deposition: investigation of material properties.** D. Hiller et al., Journal of Applied Physics (2010), 107, p 64314.

37/ **The current understanding on the diamond machining of silicon carbide.** S. Goel, J. Phys. D: Appl. Phys. (2014), 47, p 243001.

38/ **Brittle-ductile transition during diamond turning of single crystal silicon carbide.** S. Goel et al., International Journal of Machine Tools and Manufacture (2013), 65, p 15.

SiC-YiG X band quantum sensor. (J. Tribollet - 01/2019)

- 39/ **Review of laser microscale processing of silicon carbide.** B. Pecholt et al., Journal of Laser Applications (2011), 23, p 12008.
- 40/ **Solid immersion lenses for enhancing the optical resolution of thermal and electroluminescence mapping of GaN-on-SiC transistors.** J.W. Pomeroy et al., Journal of Applied Physics (2015), 118, p 144501.
- 41/ **Machining processes of silicon carbide: a review.** P. Pawar et al., Rev. Adv. Mater. Sci. (2017), 51, p 62.
- 42/ **The effectiveness of HCl and HF cleaning of Si_{0.85}Ge_{0.15} surface.** Y. Sun et al., Journal of Vacuum Science and Technology A (2008), 26, p 1248.
- 43/ **Chemical and electronic passivation of 4H-SiC surface by hydrogen-nitrogen mixed plasma.** B. Liu et al., Applied Physics Letters (2014), 104, p 202101.
- 44/ **Patterned growth of crystalline Y₃Fe₅O₁₂ nanostructures with engineered magnetic shape anisotropy.** N. Zhu et al., Applied Physics Letters (2017), 110, p 252401.
- 45/ **Spin and optical properties of silicon vacancies in silicon carbide- a Review.** S.A. Tarasenko et al., Phys. Status Solidi B (2018), 255, p 1700258.
- 46/ **Highly efficient optical pumping of spin defects in silicon carbide for stimulated microwave emission.** M. Fischer et al., Phys. Rev. Applied (2018), 9, p 54006.
- 47/ **Exploiting the symmetry of the resonator mode to enhance PELDOR sensitivity.** E. Salvadori et al., Appl. Magn. Reson. (2015), 46, p 359.
- 48/ **Subpicotesla diamond magnetometry.** T. Wolf et al., Phys. Rev. X (2015), 5, p 41001.
- 49/ **Hardware-efficient variational quantum eigensolver for small molecules and quantum magnets.** A. Kandala et al., Nature (2017), 549, p 242.

SUPPLEMENTARY INFORMATIONS

The number of V_2 spins probes having the same resonant magnetic field placed at $x_{opt}=150$ nm above a given YIG nanostripe ($500 \text{ nm} \times 100 \text{ nm} \times 100 \mu\text{m}$), and within an effective width of $W_{eff}=60$ nm around $z=0$ (fig. 1b), is estimated to be at least equal to 3000, taking $C_{2D, V_2}=1/(32\text{nm})^2$. Assuming the YIG nanostripes are laterally separated by $5 \mu\text{m}$, one has an ensemble of around 500 identical YIG nanostripes over the useful square surface of the sensor estimated to be $S_u=500 \mu\text{m} \times 500 \mu\text{m}$, taking into account the spacer width. Thus, one has around $1.5 \cdot 10^6$ identical V_2 spins probes on the sensor surface which have the same resonant magnetic field at fixed microwave frequency, that means under the strong gradient produced by the nanostripes. Note also that the surface S^* associated to target spins having the same resonant magnetic field is approximately given by $S^*=(60 \text{ nm} \times 100 \mu\text{m}) \cdot 500 = 0.3 \cdot 10^{-4} \text{ cm}^2$.

The ODMR at X band of the ensemble of V_2 spins probes used for quantum sensing, is based on efficient optical pumping^{21,30,31,45,46} (fig. 4a and 4b), as well as, on efficient photoluminescence collection^{21,30,31,45,46} (fig. 4b and 4c) of the V_2 spins probes in the 4H-SiC sculpted sample, by means of a fiber bundle containing seven fibers (fig. 1a and 4c) and of a small GRIN (gradient index) microlens (fig. 1a), as described in details below.

The central fiber sends exciting light, for example at 780 nm or at 805 nm, along an optical axe common to the GRIN microlens and to the cone shape dip of the 4H-SiC substrate (45° is the half angle of the cone). The GRIN lens, 0.25 pitch plan-plan, allows collimation of the light emerging from the central fiber. Then, by means of a first refraction at the air(Helium)/SiC interface and then by means of the many total internal reflexions (TIR) occurring inside the SiC substrate ($n=2.6$) (fig.4b), the geometric configuration of the 4H-SiC sculpted sample allows many optical rays to excite the V_2 spins located on the useful sensor surface at the top of the truncated cone shape 4H-SiC island. This TIR strategy is inspired from a previous one adopted for sensors fabricated with NV centers in diamond¹⁹, but with here a different sample design, difficult to implement with diamond technology, because diamond is harder than SiC and diamond has not a single defect axis common to all spins probes, like the V_2 center in 4H-SiC (the c axis of 4H-SiC is the only axis for V_2). This new design allows both optimization of optical excitation and of photoluminescence collection in the restricted volume of an EPR tube of less than 5 mm in external diameter, as required for using standard X band pulsed EPR resonator and spectrometer. Note that the oblique incidence of the exciting light at the sensor surface (incidence angle of around 29° on sensor surface with this design), after the first refraction, provides a non zero optical electric field component parallel to the c axis and thus allows the efficient V_2 electric dipole excitation^{21,30,31,45,46}. Here, I also assume that the optical excitation power at 780 nm or at 805 nm, at the output of the central fiber, is sufficiently high to allow the full saturation of the optical transition, during OD and OP sequences. It was previously shown⁴⁶ that the optical power necessary to obtain saturation values of optical V_2 spins pumping is inversely proportional to their longitudinal spin-lattice relaxation time $T_1(T)$, at the temperature T . As $T_1(T)$ increases up to several tens of second at 5K⁴⁶, then less than 1 mW at 780 nm spread over a $1\text{mm} \times 1\text{mm}$ square sample is sufficient at 5K for obtaining such optical pumping saturation. Of course, at room temperature, much more power is required, typically more

SiC-YiG X band quantum sensor. (J. Tribollet - 01/2019)

than 100 mw⁴⁶. Thus, from the above considerations, I consider here an optical excitation efficiency for V₂ spins located on the useful sensor surface of p_{ex}=1.

The photoluminescence of excited negatively charged silicon vacancies V₂ in 4H-SiC is emitted at 915 nm at low temperature (zero phonon line^{21,30,31,45,46} at 5K). The excited V₂ electric dipoles, aligned along the c axis of 4H-SiC, emit their photoluminescence preferentially in the plane perpendicular to the c axis, which means here, at the horizontal. The edges at 45° of the truncated 4H-SiC cone shape island thus allow, by one reflexion, to direct most of the V₂ spins probes photoluminescence vertically, towards the six lateral fibers, in which it is efficiently propagated by TIR, till the infrared photoluminescence detector. In order to evaluate more quantitatively the collection efficiency of this fiber bundle based optical setup, defined as the ratio of the collected optical power over the emitted optical power by V₂ dipoles, one can use the classical model of a linear dipole aligned along the c axis for the V₂ dipole and its emission profile determined using the Pointing vector expression. Using geometric optics (see fig. 4a) and considering the various dimensions of the setup and the relevant refractive index of the materials of the setup (n_{SiC}=2.6, n_{air}=1, and for fibers n_{glass}=1.5 and NA=0.44), one can determine that almost all rays emitted by the V₂ dipoles of the useful sensor surface around the horizontal direction at +/- 10° (= π/18 radians), can, after relevant reflexions (TIR) on the 4H-SiC sample surfaces, enter into the lateral optical fibers with a sufficiently small angle such that TIR allows the propagation of those rays without loss till the end of the fibers, towards the photodetector. Considering the Pointing vector expression associated to the V₂ dipole in spherical coordinates, one can approximate the collection efficiency p_{coll} by the ratio between the emitted PL and the collected PL, assuming that the PL is collected by the fiber bundle setup when θ is comprised between (π/2 - π/18) and (π/2 + π/18).

p_{coll} is thus given by the formula:

$$p_{coll} = \left(\int \sin^3(\theta) d\theta, \pi/2 - \pi/18, \pi/2 + \pi/18 \right) / \left(\int \sin^3(\theta) d\theta, 0, \pi \right)$$

and thus one finds here p_{coll} = 0.25.

The photodetector can be a near infrared sensitive photomultiplier tube with low dark counts, or another low noise infrared photodetection setup. Here I assume a standard infrared photodetector efficiency p_{det}=0.01. Note also that the bundle is divided, outside the standard EPR cryostat (like the CF935 from OXFORD for Bruker EPR resonators), into a single fiber, the central one used for optical excitation, and into a bundle of the six lateral fibers collecting the photoluminescence, further directed towards the photodetector.

Now let us evaluate the net signal to noise ratio R of this ODPELDOR experiment and then the sensitivity of this YiG-SiC fiber bundle-based quantum sensor. Starting from the DEER experiment expression^{1,11,33}, directly related to the ODPELDOR experiment shown on fig. 5a, and considering the optical detection of V₂ spins probes and thus the last additional π/2 microwave pulse, one obtains a photoluminescence signal expression S_{pl}, integrated during T by the photodetector, given by: S_{pl} = S₀.(1-f), with S₀ = p_{ex}.p_{coll}.p_{det}.(T/T_{V2}). (N_{V2}/8) and f, a function that depends on the parameters: 2.t₁, 2.t₂, T_{id,2D}, t_d, C_{2D,T}, p_B. The function f is given by f = exp(-((2.t₁ + 2.t₂)/ T_{id,2D})^{2/3}).((1-p_B) + p_B.V_{deer}(t_d, dx, C_{2D,Target})), where V_{deer} is the standard DEER signal. It can be numerically computed using the linear approximation and shell factorization model¹¹. This model was previously introduced for calculating the standard DEER time domain signal in the case of a three-dimensional distributions of spins. Here, this model has been adapted to take into account the bidimensional random distribution of the target spins in their well-defined plane, parallel to the SiC substrate

SiC-YiG X band quantum sensor. (J. Tribollet - 01/2019)

surface. The function p_B depends on the frequency detuning between the microwave pump frequency and the target spin resonance frequency at fixed B_{0z} . Thus, $p_B=1$ on resonance, and $p_B=0$ far off resonance for an appropriate duration π microwave pulse. The function p_B is given by the usual probability transition formula describing the Rabi oscillation between the two appropriate spins quantum states under application of a microwave pulse.

In optimal experimental conditions, the Noise N_{pl} is dominated by the optical shot noise, given by $N_{pl} = (S_{pl}(p_B=0))^{0.5}$. Thus the "net signal" to "noise" ratio R is given by the formula $R = (S_{pl}(p_B=1) - S_{pl}(p_B=0)) / N_{pl}$. Thus, introducing R_{opt} , the optimal signal to noise ratio, R is given, in the general case, by: $R = R_{opt} * (1 - V_{Deer}(td, dx, C_{2D,T}))$, with R_{opt} given by the formula: $R_{opt} = (S_0)^{0.5} \cdot \exp(-((2 \cdot t_1 + 2 \cdot t_2) / T_{id,2D})^{2/3}) / (1 - \exp(-((2 \cdot t_1 + 2 \cdot t_2) / T_{id,2D})^{2/3}))^{0.5}$. Note here that $R/R_{opt} = 1 - V_{Deer}$, that is why $1 - V_{Deer}$ is plotted on fig.6. Note also that R_{opt} depends on the spin coherence time $T_{id,2D}$ of V_2 spins probes and on the parameters t_1 and t_2 used in the ODPELDOR experiment. R of course depends on the concentration of target spins $C_{2D,T}$.

Now, assuming a sensor operating with $t_1=0.5 \mu s$, $t_2=5.75 \mu s$ and $2 t_1 + 2 t_2 = T_{id,2D} = 12.5 \mu s$, and assuming $C_{2D,T} = 1/(10nm)^2$, ie sufficiently large such that when $td=5 \mu s$, $V_{Deer}(td, C_{2D,T})=0$ ie $1 - V_{Deer}(td, dx, C_{2D,T})=1$ (fig.6c top black curve), then one finds the simple following expression for the best expected signal to noise ratio: $R = (1/e) \cdot (S_0)^{0.5}$. With $p_{ex}=1$, $p_{coll}=0.25$, $p_{det}=0.01$, a V_2 radiative recombination time $\tau_{V_2}=6ns$, and around $N_{V_2}=1.5 \cdot 10^6$ V_2 spins probes having the same resonant magnetic field in the sensor (see above), and choosing a photoluminescence integration time per ODPELDOR sequence $T=6 \mu s$ for example, one finds approximately $R=260$, for a single "one shot one point" ODPELDOR experiment. The optical re-pumping time of V_2 spins is numerically evaluated to $T_{Opump} = 20 \mu s$ at 5K assuming $k_{ISC}(5K) = 1/(1700 ns)$ (see fig. 4e), but the laser pulse is assumed to last $100 \mu s$ here for safety, considering the unmeasured value of k_{ISC} at 5K (only known is $k_{ISC}(300K) = 1/17ns$ at 300K³¹, see fig. 4d). The ODPELDOR microwave pulses sequence after optical initialization of V_2 spins last around $20 \mu s$, such that the shot repetition time of full ODPELDOR is thus taken here to be $T_{exp}=120 \mu s$. Both $T_{tot,exp} = N_{shot} * T_{exp}$ and $T_{tot} = N_{shot} * T$, increase proportionally to N_{shot} , but R only increase proportionally to $(N_{shot})^{0.5}$. Assuming $N_{shot}=100$ per point and a 100 points ODPELDOR spectrum as a function of f_{pump} (1 point each 2 MHz, 200 MHz scanned), one could obtain such a 200 MHz spectrum (see fig. 6b) in 1.2 s with a signal to noise ratio $R=2600$, assuming negligible hardware and software delays for changing the pumping microwave frequency (otherwise, the experimental time is determined by those delays).

It is here also relevant to compare standard X band direct inductively detected EPR (DD-EPR) sensitivity, with the one of this quantum sensor upgraded EPR method. Assuming a 2D target spins concentration $C_{2D,T} = 1/(10nm)^2$, and estimating the surface S^* of target spins seen by V_2 spin probes and having the same resonant magnetic field to around $S^* = 0.3 \cdot 10^{-4} cm^2$ (see above), one finds that around $3 \cdot 10^7$ target spins are sensed by the V_2 spins probes in 12 ms per point (one point each 2 MHz, 100 shots per point), with $R=2600$. As in DD-EPR¹⁵ at X band one can typically measure 10^{11} spins at 300K or 10^9 spins at 3K in 1 s with $R_{DDEPR} = 3$ (assuming a 1G linewidth for spins and a 1 Hz detection bandwidth), one finds that in order to obtain $R=2600$ in 12 ms, one would need 10^{15} target spins at 300K or 10^{13} target spins at 3K with DD-EPR. The sensitivity gain on target spins number with this quantum sensor is thus comprised between 5 and 8 orders of magnitude. Note that the probe spins sensitivity is

SiC-YiG X band quantum sensor. (J. Tribollet - 01/2019)

considerably higher than the target spins sensitivity, and it could in principle reach the single V_2 probe spin sensitivity with long enough accumulation times.

Below, I also provide some results (fig. aux. 1) of the SRIM simulations of 22 keV As^+ ions implantation in the trilayer ZnO (20 nm)/SiO₂(5 nm)/4H-SiC (type n $<5.10^{15} \text{ cm}^{-3}$), allowing, after etching of ZnO and SiO₂, to produce shallow silicon vacancies around 2 nm below the surface of 4H-SiC with an average 2D concentration of $C_{2D,V2} = 1/(32\text{nm})^2$. SRIM simulations also confirms the advantage of using a trilayer and not just a ZnO/4H-SiC bilayer, because one can see on fig. aux. 2, that some Zn atoms can reach the SiO₂ layer due to the implantation process and related collisions (SiO₂ is further removed by etching), but not the SiC substrate, thus avoiding pollution with the Zn element of the SiC substrate surface, used for quantum sensing with the silicon vacancies also produced by this implantation process.

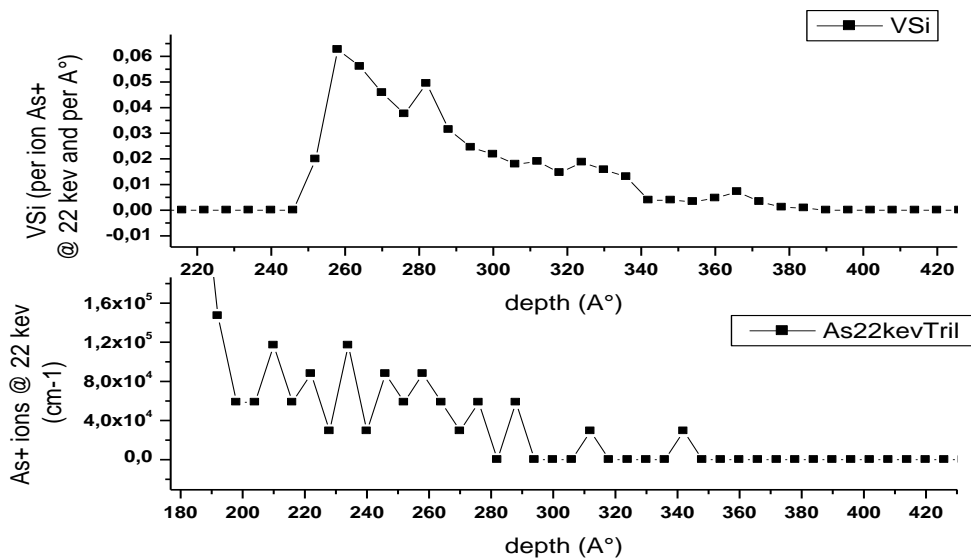


fig.Aux.1: SRIM simulation of As^+ ions implantation at 22 keV in this trilayer system (100 000 shots).

SiC-YiG X band quantum sensor. (J. Tribollet - 01/2019)

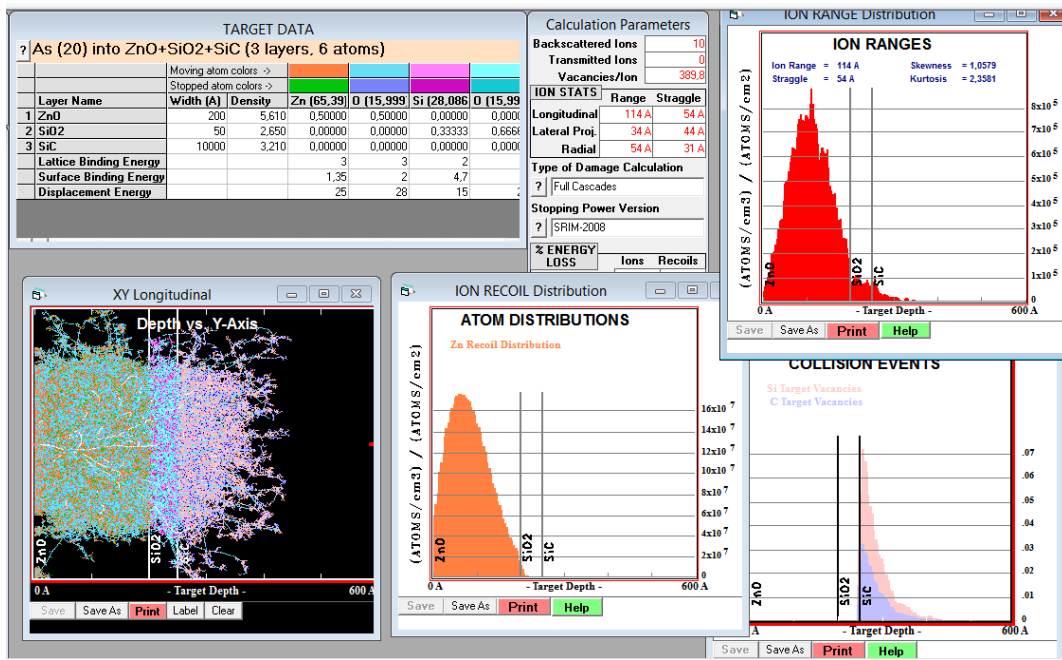


fig.Aux.2: SRIM simulation of As⁺ ions implantation at 22 keV in this trilayer system (here 6000 shots).

Below, I also provide (fig. aux. 3) a zoom of fig. 4a used for the discussion of geometric optics in the fiber bundle based ODMR setup adapted to the SiC-YiG quantum sensor described here.

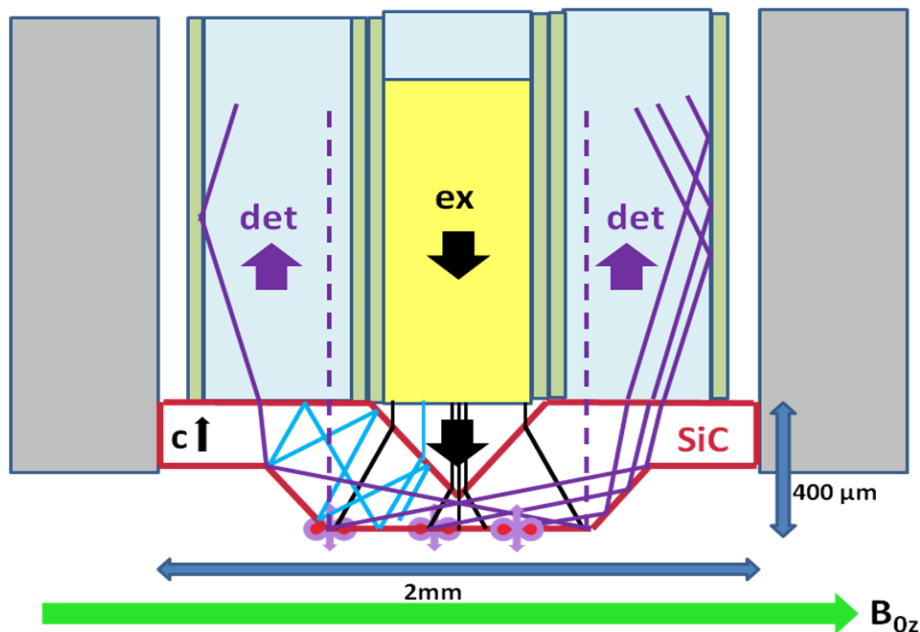


fig.Aux.3: Zoom of the setup for geometric optics analysis.